Valence state of Mn in Ca-doped LaMnO₃ studied by high-resolution Mn K_β emission spectroscopy

T. A. Tyson and Q. Qian
Department of Physics, New Jersey Institute of Technology, Newark, New Jersey 07102

C.-C. Kao and J.-P. Rueff
Brookhaven National Laboratory, Upton, New York 11973

F. M. F. de Groot*
Materials Science Center, University of Groningen, Nijenborgh 4, 9747 AG Groningen, The Netherlands

M. Croft
Department of Physics and Astronomy, Rutgers University, Piscataway, New Jersey 08854

S.-W. Cheong
*Department of Physics and Astronomy, Rutgers University, Piscataway, New Jersey 08854
and Bell Laboratories, Lucent Technologies, Murray Hill, New Jersey 07974*

M. Greenblatt
Department of Chemistry, Rutgers University, Piscataway, New Jersey 08854

M. A. Subramanian
DuPont Central Research and Development, Wilmington, Delaware 19880-0328
(Received 17 December 1998)

Mn K_β x-ray emission spectra provide a direct method to probe the effective spin state and charge density on the Mn atom and is used in an experimental study of a class of Mn oxides. Specifically, the Mn K_β line positions and detailed spectral shapes depend on the oxidation and the spin state of the Mn sites as well as the degree of d covalency/itinerancy. Theoretical calculations including atomic charge and multiplet effects, as well as crystal-field splittings and covalency effects, are used as a guide to the experimental results. Direct comparison of the ionic system MnF₂ and the covalent system MnO reveals significant changes due to the degree of covalency of Mn within atomic-type Mn K_β simulations. Moreover, comparisons of measurement with calculations support the assumed high spin state of Mn in all of the systems studied. The detailed shape and energy shift of the spectra for the perovskite compounds, LaMnO₃ and CaMnO₃, are, respectively, found to be very similar to the covalent Mn³⁺-Mn₂O₃ and Mn⁴⁺-MnO₂ compounds thereby supporting the identical Mn-state assignments. Comparison to the theoretical modeling emphasizes the strong covalency in these materials. Detailed Mn K_β x-ray emission results on the La$_{1-x}$Ca$_x$MnO₃ system can be well fit by linear superpositions of the end member spectra, consistent with a mixed-valent character for the intermediate compositions. However, an arrested Mn-valence response to the doping in the $x<0.3$ range is found. No evidence for Mn²⁺ is observed at any x values seemingly ruling out proposals regarding Mn³⁺ disproportionation. [S0163-1829(99)02231-6]

I. INTRODUCTION

The association of changes in resistivity with local structure in other oxide systems, such as the high-temperature superconductors, strongly suggests the need for a systematic study of the local electronic and atomic structure in colossal magnetoresistance (CMR) systems. The class of La$_{1-x}A_x$MnO₃ ($A=$ Ca, Sr, Ba, . . .) perovskite systems is assumed to be mixed valent [Mn³⁺($d^4,t_{2g}^3e_g^1$)/Mn⁴⁺($d^3,t_{2g}^3e_g^0$)], and exhibits many intriguing phenomena, one of which is CMR.[1] Experimentally, a direct coupling of the resistivity and bulk magnetization was found to exist.[2] It was observed by Asamitsu *et al.* that the application of an external magnetic field induced a structural phase transition in La$_{0.83}$Sr$_{0.17}$MnO₃.[3] For doping level $x>0.5$, the $A=$ Ca system (for example) becomes an antiferromagnetic insulator while for $x<0.2$ it becomes a ferromagnetic insulator (FI) persisting down to x near 0.[4] Below the insulator to metal transition temperature T_p, in the region $0.2<x<0.5$, these materials are ferromagnetic with conduction behavior characteristic of impure metals (FM—ferromagnetic metal). Above this temperature (which is close to the ferromagnetic ordering temperature T_c), the resistivity curve bends over and displays semiconductor transport characterized by carriers excited across a narrow band gap. It is found that the onset of ferromagnetism in the $x\sim1/3$ system is accompanied by a significant reduction in the resistivity[1,5] (see Ref. 5, Fig. 1). In addition, the resistivity is also reduced with the

application of a magnetic field.[1,4] It has been found that replacement of ^{16}O by ^{18}O results in a crossover from the metallic to an insulating ground state in selected materials.[6] Hence, in these materials, an intimate coupling exists between the lattice and the conduction electrons' spin and charge.

As a function of doping, using divalent cations A = Ca, Sr, Ba . . . in place of the trivalent cation La, the average valence of Mn in $La_{1-x}A_xMnO_3$ is predicted to vary continuously from Mn^{3+} ($x=0$) to Mn^{4+} ($x=1$) corresponding to a change in the d valence from d^4 to d^3. In the octahedral sites (note that the system is found to be rhombohedral or orthorhombic),[5] Mn^{3+} ions are believed to have an electron configuration, $t_{2g}^3 e_g^1$ with the t_{2g} electrons unpaired (d_{xy}, d_{xz}, and d_{yz}), and are spin polarized (according to Hund's rule) and localized on the Mn^{3+} sites. Electrons in the e_g ($d_{x^2-y^2}$ and $d_{3z^2-r^2}$) states hybridize with the $O\,2p$ states to form the conduction band. The degenerate Mn^{3+} state is known to be unstable with respect to Jahn-Teller distortions.[7–9] In local structural measurements [x-ray absorption spectroscopy (XAS) and neutron and x-ray scattering], changes in the Mn-O bond correlation or Mn-O bond distribution were found to track the onset of the ferromagnetic conducting state.[10]

In Zener's original double-exchange model[11] for this system, the lattice is assumed to be rigid and ferromagnetism is induced by a spin coupling of the Mn^{4+} nearest-neighbor sites mediated by the e_g conduction electrons. Many recent experimental reports assume an ionic mixed-valence state of Mn in these materials—a central ingredient of double-exchange theory. However, there has been no systematic exploration of the exact valence and spin state of Mn in these systems. The purpose of this paper is to explore this area from the experimental perspective.

There is much conflicting data on the valence of Mn. In thermoelectric power experiments (TEP), Hundley and Neumeier[12] find that more holelike charge carriers or alternatively fewer accessible Mn sites are present than expected for the value x. They suggest a charge disproportionation model based on the instability of Mn^{3+}-Mn^{3+} relative to that of a Mn^{2+}-Mn^{4+}. This transformation provides excellent agreement with doping-depend trends exhibited by both TEP and resistivity. Using electron paramagnetic resonance (EPR) measurements, Oseroff *et al.*[13] suggest that below 600 K there are no isolated Mn atoms of valency +2, +3, or +4. However, they argue that EPR signals are consistent with a complex magnetic entity composed of Mn^{3+} and Mn^{4+} ions. Park *et al.*,[14] based on $Mn\,2p$ x-ray photoelectron spectroscopy (XPES) and $O\,1s$ absorption, support the double-exchange theory with mixed-valence Mn^{3+}/Mn^{4+} ion. They were able to obtain approximate spectra of the intermediate doping XPES spectra by linearly combining the end-member spectra—consistent with a linear change of spectral features with doping. However, the significant discrepancy between the weighted spectrum and the prepared spectrum (for given x) suggests a more complex doping effect. Subias *et al.*[15] examined the valence state of Mn utilizing Mn K-edge x-ray absorption near edge spectra (XANES). Again, a large discrepancy is found between intermediate doping spectra and linear combinations of the end members. They suggest that Mn does not fluctuate between 3+ and 4+ (not ionic) and

find a unique magnetic signature for Mn using x-ray magnetic dichroism measurements. Systematic shifts in the absorption edge position with doping have been found by Subias *et al.* (Mn K edge),[15] Booth *et al.* (Mn K edge),[10(c)] Croft *et al.* (Mn K edge),[16(a)] Liu *et al.* (Mn L edge), and Pellegrin *et al.* (Mn L edge and O K edge).[17] We point out that in true mixed-valence ionic systems such as $Sm_{1-x}Eu_xS$ or $SmSe_{1-x}Sb_x$, clear resonance lines are seen for each distinct valance state.[18] In addition, a significant shift in the edge position with doping is found. This set of conflicting CMR data suggests the need for an in-depth exploration of the valence state of Mn in this perovskite system.

In order to clarify the nature of the valence state of Mn in these systems, we have performed systematic Mn K_β emission measurements. The Mn K_β emission spectrum provides a direct method to probe the total Mn $3d$ spin S and effective charge density on the Mn sites. The main line position depends both on the oxidation and the spin state of Mn. The details of the multiplet structure depend on the spin alignment (high spin vs low spin) and point group symmetry of the Mn site (crystal-field effects) to a lesser extent.[19–21]

Measurements of the emission spectra have been complemented by detailed multiplet structure modeling.[19(a), 19(b)] Unlike absorption edge measurements, the spectra yield information (main line positions and detail shapes) of the Mn sites that is not significantly affected by the geometry of the ligands. The changes in coordination and local structure that accompany changes in valence have less of an impact on emission measurements. Consequently, this approach is well suited to address the question of the nature of the valence of Mn in the CMR system.

II. EXPERIMENTAL METHODS

Samples of $La_{1-x}Ca_xMnO_3$ series were synthesized and characterized as described in Ref. 16(a). Samples from the same preparation sets were used in our experiments. The powder samples were prepared by methods similar to those used in other studies, for which a large body of transport and magnetic measurement exists in the literature. The $CaCu_3Mn_4O_{12}$ material was prepared as described in Ref. 16(b). Fluorescence measurement samples were prepared by finely grinding the material and packing it onto adhesive tape.

The Mn K_β fluorescence measurements were performed at the National Synchrotron Light Source's (NSLS) 27 pole wiggler Beamline X21A. The experimental setup, which consists of an analyzer and detector in Rowland geometry, is described in Ref. 22 and the measurements were performed in a manner analogous to that of Refs. 19(a) and 23. An incident energy ($\hbar\omega$) of 6556 eV was selected using a four-bounce Si (220) monochromator. [Measurements at incident energies of 6566, 6700, and 9000 eV yielded the same trends. However, the 6556 eV spectra yielded the most narrow line shapes.] The incident energy was calibrated by the known Mn metal K-edge absorption inflection point (6539 eV). A spherically bent Si (440) crystal analyzer was used to resolve the energy of the emitted photons, $\hbar\Omega$. A solid-state Ge fluorescence detector was used to measure the fluorescence radiation. The absolute fluorescence photon energy

was calibrated from the elastic scattering peaks of the sample at the same position utilizing the known incident energy. Spectra reported here are the average of 5–7 scans. Error bars are determined by assuming a Gaussian distribution in the number of counts at each energy point.

The MnF$_2$ K_β spectrum was used as a reference to check the stability of the spectrometer during measurement. It was found that the spectrometer was quite stable and the position of the main peak in the MnF$_2$ spectrum was always reproducible to better than 0.1 eV. The incident energy was found never to shift by more than 0.2 eV during experiments. All data are corrected by an efficiency function that is obtained from the elastic measurement in the same energy range. The energy resolution is determined by the elastic scattering line full width at half maximum that was approximately 0.5 eV for the energy range measured.

In the emission measurements, the energy calibration of the spectrometer is sensitive to the sample positioning. Accordingly, when changing samples, the detector position was always checked by an alignment scan to confirm that the detector was correctly aligned. The x-ray absorption spectra, reported here, were measured at beam line X19A at NSLS in fluorescence mode as described in Ref. 16(a).

III. COMPUTATIONAL METHODS

The computations for the Mn K_β fluorescence spectra are based on atomic and crystal-field theory. In this model, we take account for the effective exchange splitting as well as all possible couplings of the angular momenta (orbital and spin) of all electrons outside of closed shells or holes in filled shells. Additional energy splittings from a cubic crystal field, from $3d$ spin-orbit coupling and from Jahn-Teller distortion are also considered in our calculation. Similar calculation methods have been reported by Peng et al.,[19(a)] Wang, de Groot, and Cramer,[20] and de Groot et al.[21] The parameters used in the calculation are the $3p3d$ and $3d3d$ Slater integrals, and the $3p$ as well as $3d$ spin-orbit couplings. The atomic value for Slater integrals were obtained from the Hartree-Fock method scaling them by factors of 80% and 60%. An 80% reduction is a standard scaling used to correct the overestimated values obtained from the Hartree-Fock approximation.[19(b)] A reduction factor of 60% was also used in this work to explore the effects of covalency. In order to make comparisons with the experimental spectra, the calculated spectral lines were convoluted with a Lorentzian that reflects lifetime broadening and with a Gaussian that accounts for experimental broadening. Absolute energy positions cannot be obtained from these calculations.

IV. RESULTS AND DISCUSSION

A. Mn K_β emission structure

To address the spectral shape of the Mn K_β emission spectra presented here, consider the photoionization excitation of a Mn atom in a solid by an x-ray photon. Since dipole photoexcitation is spin invariant, the creation of a core hole of spin-up or spin-down symmetry (relative to the total $3d$-band spin) are equally likely. In the $3p \rightarrow 1s$ decay process (K_β emission), the coupling between the $3p$ hole (or $3p$ electron spin now left unpaired) and the $3d$ electrons pro-
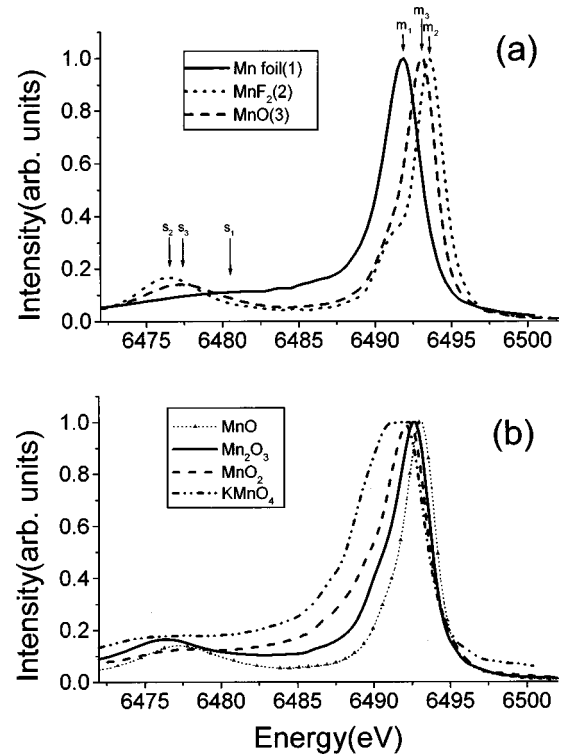

FIG. 1. (a) Mn K_β spectra of the standard materials: elemental Mn, ionic-2+ MnF$_2$, and covalent-2+ MnO. The main (m) and satellite (s) lines for the different spectra are noted. (b) Mn K_β spectra of the standard materials: MnO, Mn$_2$O$_3$, MnO$_2$, and KMnO$_4$. All data shown are smoothed by five point Fourier filtering.

duce two possible final states of different energies. One observes (in Mn^{3+} for example) differences in the energy of the coupled spin-down $3p$ hole $[\Psi(3p(\uparrow)3d^4)]$ state and spin-up hole state $[\Psi(3p(\downarrow)3d^4)]$. For a fixed incident photon energy $\hbar\omega$ above the Mn K-edge, the K_β emission spectrum of photons $\hbar\Omega$ can be resolved into these two components—a main line (m) and a satellite line (s) [see, for example, the m and s lines in Fig. 1(a)]. Qualitatively, it is found that the energy splitting between the main line and satellite is given by $\Delta E_{sm} = J(2S+1)$ while the intensity ratio of the satellite to the main peak is given by $I_s/I_m = S/(S+1)$, where S is the total spin of the unpaired electrons in the $3d$ shell and J is the exchange integral.[19(c)]

These main and satellite lines are illustrated in Fig. 1(a), where the Mn K_β emission spectra for elemental Mn (Mn^0), MnF$_2$ (Mn^{2+} ionic), and MnO (Mn^{2+} covalent) are shown. The ΔE_{sm} splitting dominates the m-line position in these materials. The relatively small ΔE_{sm} and washed out satellite of the Mn-metal spectrum reflects the $3d$-itinerancy reduction in the intra-atomic Mn-$3d$ interactions. In contrast the localized atomiclike $3d$ states in the Mn^{2+} ionic, MnF$_2$ compound yield a large ΔE_{sm} splitting and robust satellite structure. The covalency reduction in the ΔE_{sm} splitting and satellite sharpness in the covalent-Mn^{2+}, MnO spectrum is clear when compared to the ionic-Mn^{2+} case. As will be discussed in the modeling section, it is not just the ΔE_{sm} splitting and satellite sharpness that is sensitive to the Mn spin and charge state. Indeed, there are multiple satellite contributions to the spectra that also vary strongly with the Mn
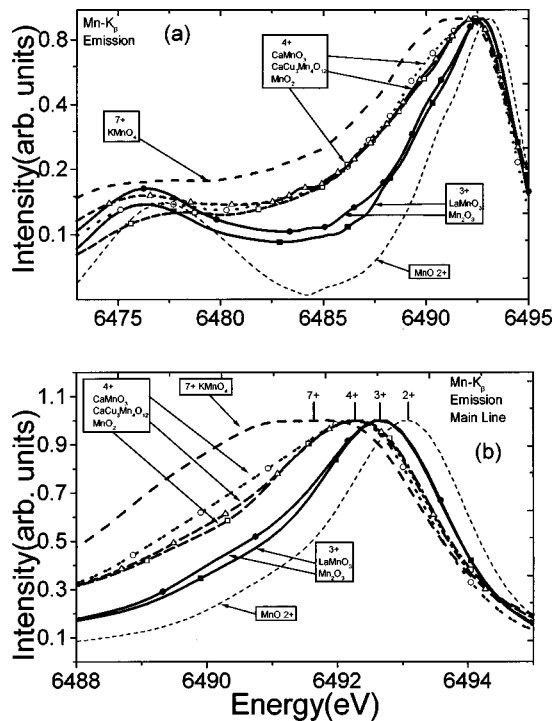
FIG. 2. (a) Comparison of the Mn K_β spectra of a series of covalent oxide compounds. MnO (2+), Mn_2O_3 (3+), $LaMnO_3$, MnO_2 (4+), $CaMnO_3$, $CaCu_3Mn_4O_{12}$, and $KMnO_4$ (7+). The logarithmic intensity scale is used to facilitate comparisons of the weak satellite as well as the main lines. Note the clustering of the curves into groups by the Mn valence. (b) An enlargement (on a linear scale) of the main line peak region of the spectra in the previous figure. Note the coincidence of the main line peaks for compounds with the same Mn valence.

FIG. 3. (a) Mn K-edge x-ray emission spectra for the oxides: Mn_2O_3, MnO_2, $LaMnO_3$, and $CaMnO_3$. (b) The corresponding x-ray absorption spectra. Note that in the case of the emission spectra, a more direct comparison of the spectra can be made to determine the valence state of Mn.

spin and charge state. In Fig. 1(b), the corresponding spectra for the 3+, 4+, and 7+ models are shown (note that all oxides are octahedrally coordinated except $KMnO_4$, which is tetrahedral). Below we will show that we can group the oxides according to valence states.

In addition to these intra-atomic exchange couplings there is also a smaller chemical shift in the Mn K_β line energy due to the loss of core screening that accompanies loss of localized $3d$ character. Although both the initial $3p$ and final $1s$ states will shift to higher binding energy with Mn-$3d$ screening loss, the Mn-$3p$ shift is larger. Thus loss of local Mn-$3d$ charge should lead to a lowering of the Mn K_β emission energy.[19(d)]

B. Mn K_β emission—Mn valence correlation in oxides

Considering the multiplet structure effects that combine to yield the Mn K_β energy position and shape, the utility of this spectroscopy for probing the Mn-valence state in a class of oxide materials will be addressed first. In Fig. 2(a) the Mn K_β spectra for a group of covalent Mn oxide compounds with varying formal valences are shown. A logarithmic intensity scale is used in this figure to aid in comparing the weak satellite region.

In Fig. 2(b) the vicinity of the main peak for these compounds is displayed on a linear scale. The MnO (2+), Mn_2O_3 (3+), and MnO_2 (4+) binary standard compounds all have
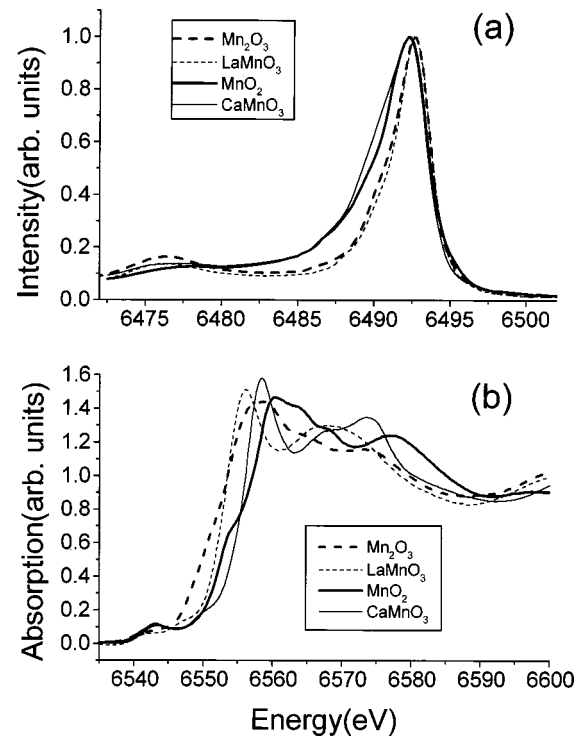
Mn in an octahedral environment while the $KMnO_4$ (+7) standard is tetrahedral. The perovskite $LaMnO_3$ (3+) and $CaMnO_3$ (4+) compounds, of course, also have octahedral Mn-O coordination. Finally the quadrupled, distorted-perovskite $CaCu_3Mn_4O_{12}$ compound also has octahedral Mn coordination and has been recently shown to be a Mn(+4) compound.[16(b)]

Figures 2(a) and 2(b) emphasize that, for this rather broad group of materials, the spectra cluster into classes of curves that are determined by their valence. Specifically, the energy of main peak maximum, the spectral broadening on the high-energy side of the main line, the depth of the spectral minimum between the main and satellite line, and the sharpness of the satellite line are all quite consistent for oxides in this group with the same formal Mn valence [see Ref. 19(e)]. Thus it is evident from Figs. 2(a) and 2(b) that (for such related oxides) different Mn valence states produce distinct Mn K_β spectra and one can thereby make a Mn valence state determination. (The model spectra reported here were found to be consistent with spectra on the nonperovskite related standard compounds measured by Bergmann *et al.*[24]) Moreover, Mn^{3+} and Mn^{4+} states for the end-point perovskites, in the $La_{1-x}Ca_xMnO_3$ series are also supported by these results.

To emphasize the utility of this Mn K_β method of valence estimation, the emission spectra of $LaMnO_3$, $CaMnO_3$, Mn_2O_3, and MnO_2 [Fig. 3(a)] are compared with the Mn K-edge absorption spectra of the same materials [Fig. 3(b)]. The gross shapes of the 3+ and 4+ emission spectra for the standard and CMR systems are quite similar. (Hence the above noted Mn is in a 3+ state in the $LaMnO_3$ and in a 4+ state in $CaMnO_3$.) This simplicity is in contrast to the
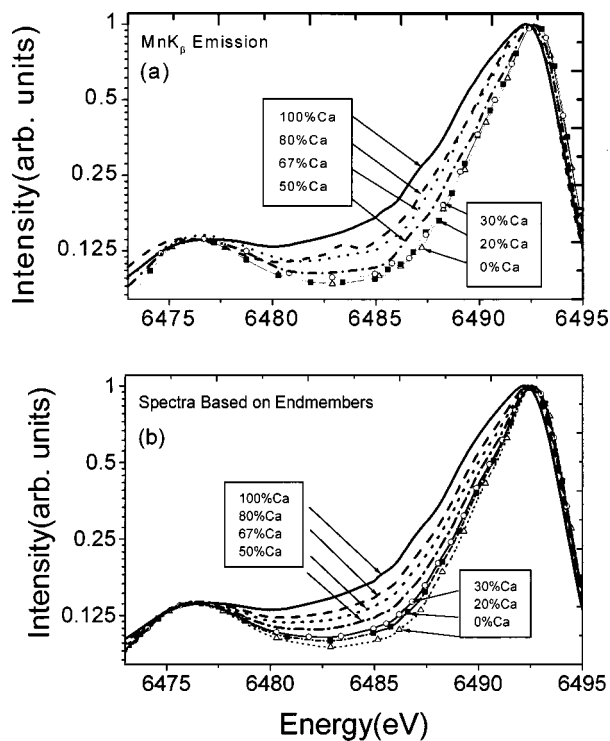
FIG. 4. (a) Mn K_β spectra of La$_{1-x}$Ca$_x$MnO$_3$ perovskites system with different Ca doping: $x = 1.0, 0.8, 0.67, 0.5, 0.3, 0.2, 0$. (b) Mn K_β spectrum based on combinations of the two end member spectra for all dopings in (a).

K-edge absorption measurements shown in Fig. 3(b) (see also Subias et al.[15] and Croft et al.[16(a)]) (In general, the near-edge absorption spectrum is strongly affected by the local structure about the absorbing atom.) The near K-edge absorption edges of the binary standards manifest double step rises due to the details of the p component of the electronic structure of these compounds. Although the coincidence of the midpoints of the two-step rise of the 3+ and 4+ model absorption curves with those of the end-point perovskite compounds is sufficient to infer similar valences, the decisiveness of this conclusion is not as direct and is more compound-detail dependent than the emission conclusion.

C. Mn K_β emission for the La$_{1-x}$Ca$_x$MnO$_3$ system

In Fig. 4(a) we show the emission spectra for the La$_{1-x}$Ca$_x$MnO$_3$ perovskites system with different Ca doping. Note the systematic shift in the main line position with increasing oxidation state. Similar systematic shifts in peak positions are found by forming linear combinations of the end members [Fig. 4(b)]. Although qualitative trends can be seen by looking at the raw spectra, a quantitative approach was found. First, the end member spectra (i.e., $x = 0$ and 1) were each fit a sum of four Voigt functions (to model the complex multiplet structure), the distribution of which were chosen both from the theoretical modeling and from the spectral shapes. (Fits with very small χ squared values were obtained.) The results of this fitting procedure for the end member perovskites are presented in Table I along with the results of similar fits for the other standard compounds (discussed below). The fitted functional forms for the end members were then combined with the relative weights w_{La} and

w_{Ca} [with $w_{La} + w_{Ca} = 1.0$] to model the intermediate-x spectra. The single weight parameter w_{Ca} was then allowed to vary to give the best least-squares fit to the intermediate spectra.

The absolute intensity ratio of the end point spectra had to be fixed in this modeling. Relative end member normalizations based on the 50%, 67%, and 80% [i.e., assuming the end-point intensity ratio was given by $x/(1-x)$] were each tried. The fitted x dependence of the w_{Ca} weight for each of these normalizations are shown in Fig. 5. The x dependence of this weighting can be seen to show a similar variation for all three choices of normalization.

It is interesting to note that the fitted variation of w_{Ca} is not simply equal to x as one would expect from a purely linear variation in the Mn valence with x. Indeed, above $x \sim 0.3$ (Ca doping), one finds linear behavior with the expected slope while below $x \sim 0.3$ the slope is almost flat. The x variation of the Mn K-edge XAS chemical shift and pre-edge feature area (both indicators of Mn-valence variation) manifest a similar two region behavior.[16(a)] Indeed the effective unit cell volume also shows a similar behavior. These results again raise the question of whether there is an arrested Mn-3d hole variation, for low values of Ca substitution, in this system.

D. Fits to Mn K_β emission spectra

The method of fitting the Mn K_β emission spectra to a superposition of symmetrically peaked features has been applied to the other pure compound spectra considered here. The 2+ Mn compound spectra were well fit by three features, as illustrated in Fig. 6(a) for the case of MnF$_2$. In this case, Lorentzian functions were used to fit the experiment spectra, since the peak width is mainly dependent on the 3p hole width that is much broader than the Gaussian experimental width of $\sim$0.5 eV of our spectrometer. (Fits to Voigt function produce very similar results.) It is clear that there are three peaks at 6493.6, 6491.0, and 6476.6 eV. The black dots represent the experiment data with error bars, the solid line is the sum of total fit of all components, and all other lines are individual Lorentzian fitting lines. The comparison to the theoretical calculations for the Mn K_β emission spectrum [Fig. 6(b)] will be discussed in the calculations section.

The fitting parameters for all fits to all of the pure compound spectra are presented in Table I (Note that all of the fit parameters reported in Table I used Lorentzian line components.) Besides yielding the energies of the potential component features in these spectra, this fitting procedure yields the net and individual feature integrated spectral areas. The 3d-3p interactions are certainly responsible for the dramatic Mn K_β spectral variations seen above. However, to the first approximation, the 3p states are core states and therefore the integrated oscillator strength of the 3p-1s transitions should not vary with the Mn-3d configuration. Therefore, the integrated intensities of the fitted functions could provide the normalization factors with which the spectra discussed here could be rescaled to the constant oscillator strength approximation. Although this rescaling is not performed here, the net spectral areas are reported for this reason. The fitted function results are also reported to provide a useful method

TABLE I. Lorentz parameters for Mn K_β spectra.

Sample	Peak	Position	Area	Height	Width
Mn foil	Peak 1	6492.0(0.05)	2.90(0.42)	0.854(0.156)	2.17(0.10)
	Peak 2	6490.7(0.23)	1.16(0.54)	0.256(0.141)	2.66(0.51)
	Peak 3	6486.3(0.41)	0.74(0.38)	0.065(0.017)	6.18(2.17)
	Peak 4	6478.6(0.73)	1.52(0.35)	0.111(0.011)	11.1(2.01)
MnF$_2$	Peak 1	6493.6(0.01)	2.79(0.05)	0.953(0.009)	1.87(0.03)
	Peak 2	6491.0(0.06)	0.67(0.06)	0.189(0.007)	2.30(0.20)
	Peak 3	6476.6(0.14)	1.34(0.07)	0.162(0.007)	5.52(0.43)
MnO	Peak 1	6493.1(0.02)	2.49(0.16)	0.916(0.030)	1.75(0.06)
	Peak 2	6491.6(0.15)	1.13(0.19)	0.234(0.024)	2.87(0.25)
	Peak 3	6477.4(0.22)	1.50(0.10)	0.146(0.006)	7.34(0.68)
Mn$_2$O$_3$	Peak 1	6492.8(0.03)	2.52(0.25)	0.853(0.052)	1.84(0.09)
	Peak 2	6491.0(0.14)	1.67(0.48)	0.360(0.049)	3.02(0.53)
	Peak 3	6486.7(1.04)	0.62(0.45)	0.065(0.019)	6.96(3.65)
	Peak 4	6476.4(0.28)	1.91(0.27)	0.175(0.008)	8.07(1.20)
MnO$_2$	Peak 1	6492.4(0.05)	2.95(0.52)	0.744(0.152)	2.23(0.17)
	Peak 2	6490.7(0.22)	1.80(0.95)	0.388(0.186)	3.24(0.92)
	Peak 3	6487.6(0.51)	1.08(0.60)	0.193(0.088)	4.72(1.49)
	Peak 4	6477.9(0.56)	1.88(0.38)	0.139(0.007)	10.67(2.36)
LaMnO$_4$	Peak 1	6492.7(0.02)	2.77(0.20)	0.905(0.038)	1.93(0.08)
	Peak 2	6490.8(0.16)	1.33(0.35)	0.268(0.034)	3.16(0.55)
	Peak 3	6484.7(1.26)	0.61(0.49)	0.059(0.017)	8.66(5.71)
	Peak 4	6476.3(0.35)	1.33(0.33)	0.142(0.013)	6.75(1.53)
CaMnO$_4$	Peak 1	6492.4(0.04)	2.40(0.33)	0.747(0.081)	1.94(0.14)
	Peak 2	6490.5(0.12)	2.53(0.81)	0.506(0.113)	3.20(0.61)
	Peak 3	6486.8(0.97)	1.21(0.86)	0.147(0.074)	6.79(2.87)
	Peak 4	6476.7(0.57)	1.82(0.53)	0.152(0.010)	9.61(2.81)
CaCu$_3$Mn$_4$O$_{12}$	Peak 1	6492.4(0.04)	2.89(0.35)	0.740(0.080)	2.22(0.13)
	Peak 2	6490.4(0.17)	2.08(0.74)	0.447(0.087)	3.49(0.73)
	Peak 3	6486.4(0.79)	1.06(0.68)	0.096(0.042)	6.52(2.54)
	Peak 4	6476.3(0.49)	2.24(0.43)	0.174(0.014)	10.75(2.03)
KMnO$_4$	Peak 1	6492.5(0.06)	1.85(0.39)		1.88(0.18)
	Peak 2	6490.9(0.09)	1.93(1.01)		2.23(0.62)
	Peak 3	6489.3(0.23)	1.70(0.89)		2.81(0.67)
	Peak 4	6485.6(0.93)	1.26(0.67)		7.72(2.68)
	Peak 5	6476.2(0.59)	1.40(0.40)		8.81(2.36)

for other workers to replicate these results for comparison to results on other materials or more detailed theories.

E. Theoretical Mn K_β calculations

An example of the results of an atomic multiplet plus an octahedral crystal field (of magnitude $10Dq = 1.5$ eV) calculations for the Mn K_β emission spectrum for Mn^{2+} is shown in Fig. 6(b). The decomposition of the emission spectra into spin-up and spin-down components (relative to the $3d$ moment) is also given. Note the very close similarity between the measured MnF$_2$ spectrum [Fig. 6(a)] and the model spectrum. A scaling factor of 80% for the Slater integrals was used. There are three peaks, the main peak, a low energy shoulder at ~3 eV below the main peak, and a satellite peak at ~17 eV below the main peak. The splittings are comparable to the fitted feature splittings for MnF$_2$ shown in Table I.

As noted earlier, the comparison of the Mn, MnF$_2$, and MnO results the ΔE_{sm} splitting is sensitive to the degree of compound covalency. In the initial model calculations, it was found that the 80% and 60% Slater integral reduction yielded results that bracketed the experimentally observed ΔE_{sm} splittings. Consequently, the following theoretical studies of the Mn-valence and crystalline electric-field influences on the Mn K_β emission spectra were carried out at these two levels of covalency reduction.

In Fig. 7(a) the systematic computations of the Mn^{2+} emission spectra, with $10Dq$ varying from 0 to 3 eV, show no change in spectral shape. The onset of the high-spin to low-spin transition (characterized by a dramatic reduction of the satellite), occurs at a higher crystal-field parameter with a larger scaling [low covalency, see Fig. 7(a)]. The spectra are consistent with MnF$_2$ in a high spin state as expected. In our calculations, $10Dq$ (crystal-field splitting parameter) was varied from 0 to ~3.9 eV. When $10Dq$ reaches 3.3 eV, the K_β spectrum switches to low spin from the previous high spin state and the main peak position shifts to lower in energy. The spectrum becomes stable at 3.3–3.9 eV. The
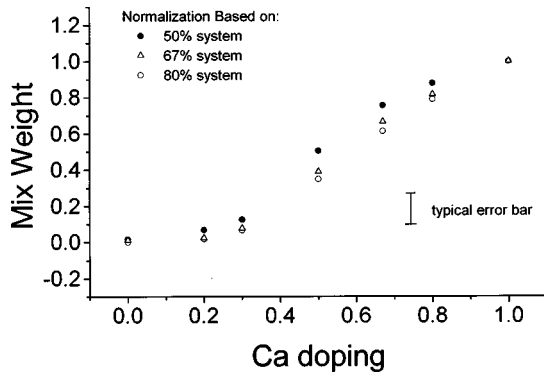
FIG. 5. Fitted weight w_{Ca} in the equation $w_{Ca}*CaMnO_3+(1-w_{Ca})*LaMnO_3$ as a function of the Ca doping, x. Note the two-region doping behavior of the oxidation of the Mn sites as a function of Ca content. A typical error bar for the points is shown. The w_{Ca} determinations based on normalization fixed by the 50%, 67%, and 80% sample spectra are all shown. Note the basic shape of the w_{Ca} variation with x is independent of the end member normalization procedure. The boundary between the regions seems to coincide with crossover from ferromagnetic metal to ferromagnetic insulator behavior.

broadening of the satellite in experiment is due to the short lifetime of the $3p$ spin-up hole state.[20] (Note that further reductions in symmetry do not significantly change the main line profile.) In Fig. 7(b), we show the computed spectra for a Slater scaling parameter of 60% (more covalent). Note the
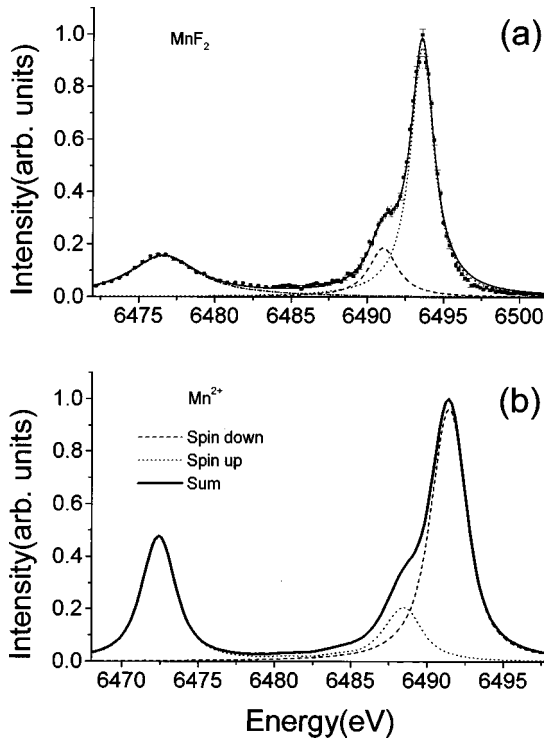
FIG. 6. (a) Example of raw data and fits. MnF$_2$ (Mn^{2+}) K_β spectrum with Lorentzian function fitting. Solid line is the sum of all components of fit. The fitting parameters including widths and peak positions for all spectra are given in Table I. (b) The calculated Mn K_β spectrum of Mn^{2+} ($10Dq=1.5$ eV) showing the decomposition into mainly spin-up and mainly spin-down $3p$ hole components relative to the $3d$ moment.
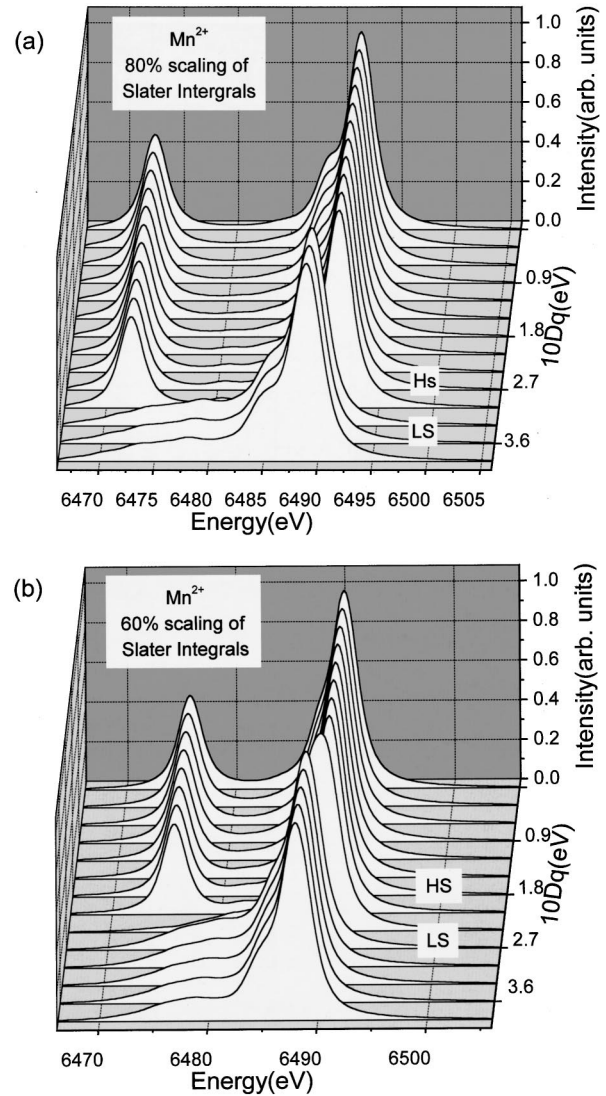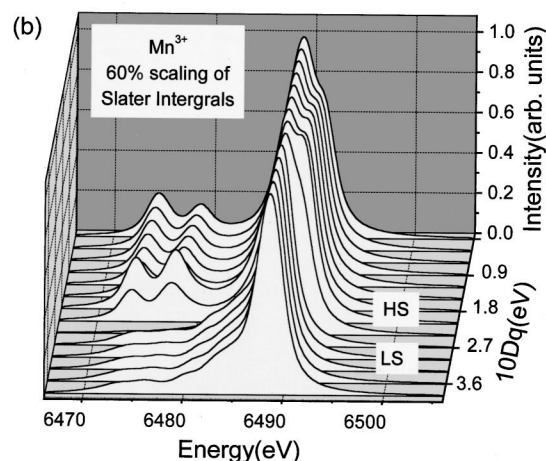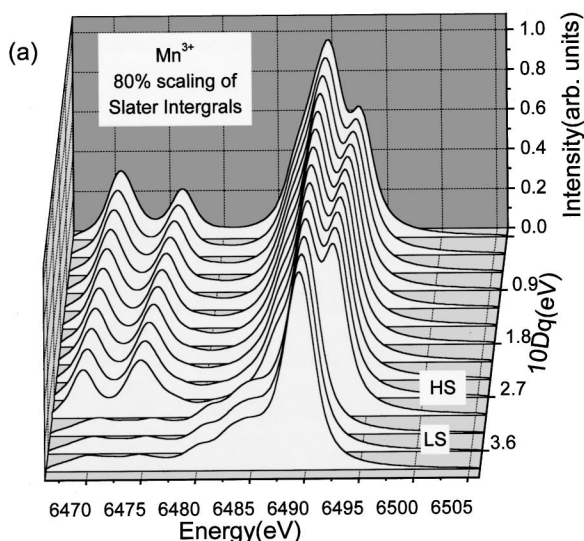

FIG. 7. (a) Calculated Mn^{2+} K_β multiplet crystal-field spectrum with $10Dq$ ranging from 0 to 3.9 eV and Slater integrals scaled to 80%. The Lorentzian broadening is 1.0 eV and the Gaussian broadening is 0.5 eV. (b) Calculated Mn^{2+} K_β multiplet as in Fig. 7(a) but with 60% scaling of Slater integrals. Note the differences in splittings and relative intensities of the major peaks. Smaller Slater integrals (effect of higher covalency) reduce peaks separation and produce smoother peak profiles. Compare MnO with MnF$_2$.

change in splittings and the relative intensity of the shoulder to the main line. The separation between the main peak and the satellite peak decreases when the scaling factor decreases (or covalency increases).

Figures 8(a) (80% scaling) and 8(b) (60% scaling) display the multiplet crystal-field calculations for Mn^{3+} with octahedral symmetry. The onset of the high- to low-spin transition does not occur until $10Dq$ equals 3.0 and 2.1 in the 80% and 60% scaling models, respectively. With low covalency (80% scaling) there is a large shoulder on the high-energy side of the main peak. This is significantly reduced when covalency is increased by reducing the scaling of the Slater integrals. In fact, this shoulder is not seen in the Mn$_2$O$_3$ spectrum. The satellite intensity is also significantly reduced with increased covalency—consistent with the observed Mn$_2$O$_3$ spectra.

FIG. 8. (a) Calculated Mn^{3+} K_β multiplet crystal-field spectrum with $10Dq$ ranging from 0 to 3.9 eV and Slater integrals scaled to 80%. The Lorentzian broadening is 1.0 eV and the Gaussian broadening is 0.5 eV. (b) Calculated Mn^{3+} K_β multiplet as in Fig. 8(a) but with 60% scaling of Slater integrals.

FIG. 9. (a) Calculated Mn^{4+} K_β multiplet crystal-field spectrum with $10Dq$ ranging from 0 to 3.9 eV and Slater integrals scaled to 80%. The Lorentzian broadening is 1.0 eV and the Gaussian broadening is 0.5 eV. (b). Calculated Mn^{4+} K_β multiplet as in Fig. 9(a) but with 60% scaling of Slater integrals.

Figures 9(a) (80% scaling) and 9(b) (60% scaling) display the multiplet crystal-field calculations for Mn^{4+} with octahedral symmetry. There is no high spin to low spin transition with $10Dq$ varying from 0–3.9 eV. The main line becomes sharper with increasing $10Dq$ and increased covalency. The separation between the main line and the first low-energy shoulder decreases with increased covalency. In fact, in the standard spectra for MnO_2, the shoulder is merged with the main line. Hence the oxides MnO, Mn_2O_3, and MnO_2 are highly covalent as expected. The variations between the emission spectra of $CaMnO_3$ and MnO_2 in Fig. 3(a) are due to the difference in covalency between the two systems, with $CaMnO_3$ being somewhat less covalent.

V. SUMMARY AND CONCLUSIONS

$Mn K_\beta$ x-ray emission spectra provide a direct method to probe the total $Mn 3d$ spin S and effective valence on the Mn sites. The $Mn K_\beta$ main line positions and spectral shapes depend on the oxidation state, the spin state, and the itinerancy/covalency of the Mn sites. Direct comparison of
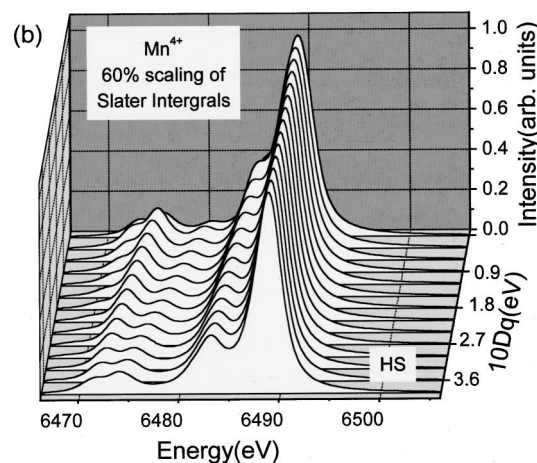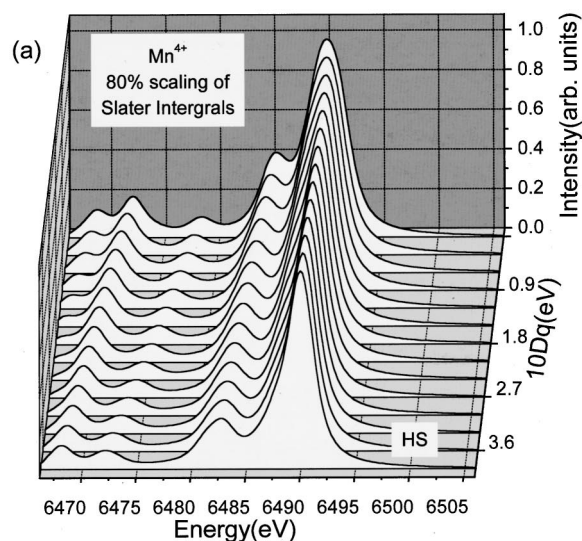
the ionic system MnF_2 and the covalent system MnO reveals significant changes due to the degree of covalency of Mn. Atomic-type $Mn K_\beta$ simulations are consistent with these findings and support the assumed high spin state of Mn in these systems.

For a rather broad class of Mn-oxide materials the $Mn K_\beta$ emission technique appears to provide a valid and structure insensitive indicator of the Mn-valence state. In this way, the $Mn K_\beta$ emission method could provide a substantial improvement over the empirically useful but structure sensitive $Mn K$-edge XAS technique. In particular the $Mn K_\beta$ emission results show the $LaMnO_3$ and $CaMnO_3$ to be covalent Mn^{3+} and Mn^{4+}, respectively, by a clear comparison with Mn^{3+}-Mn_2O_3 and Mn^{4+}-MnO_2 covalent oxide standards. The $Mn K$-edge XAS studies have yielded a similar Mn-valence state conclusion but with a comparison that was less straightforward. Moreover, the magnitude of the main-satellite line splitting in the $Mn K_\beta$ emission results (compared to the covalency reduction factors required to theoretically model comparable splittings) further emphasize the strong covalent character of these perovskite materials. In

addition, the main line to satellite ratio gives information about the spin alignment of the d levels on the Mn sites.

Regarding the $La_{1-x}Ca_xMnO_3$ system, the Mn K_β emission results are consistent with a mixed valent Mn^{3+}/Mn^{4+} mixing that scales with the composition except for the $0 < x < 0.3$ range where the Mn-valence response appears arrested (with the apparent hole doping being nearly constant for $x < 0.3$). Indeed the intermediate ($0.3 < x < 0.9$) spectra are well represented by linear superpositions of the $x = 0$ and 1 end-point spectra in direct proportion to x. By contrast, this Mn K_β emission superposition method is inconsistent with Ca content below $x \sim 0.3$. This is the compositional range where the order switches from FI to FM, and the origin of the arrested Mn-valence response at low x is potentially important. Finally, for the $La_{1-x}Ca_xMnO_3$ system, the Mn K_β emission results show absolutely no evidence for Mn^{2+} (which would have a quite distinct emission spectrum) and would appear to rule out the Mn^{2+}-Mn^{4+} disproportion mechanism.[12] Interestingly, while Mn K-edge XAS results evidence an average Mn-valence x variation (for $La_{1-x}Ca_xMnO_3$), the intermediate-x XAS spectra are far too sharp to be modeled by a superposition of the end-point spectra.[15]

*Present address: Department of Inorganic Chemistry of the University of Utrecht, Sorbonnelaan 16, 3584 Utrecht, The Netherlands.

[1] (a) R. von Helmolt, J. Wecker, K. Samwer, L. Haupt, and K. Bärner, J. Appl. Phys. **76**, 6925 (1994) and references therein; (b) J. B. Goodenough and J. M. Longon, *Magnetic and Other Properties of Oxides and Related Compounds*, Landolt-Börnstein, New Series, Group III, Vol. 4, Pt. a (Springer-Verlag, Berlin, 1970).

[2] M. F. Hundley, M. Hawley, R. H. Heffner, Q. X. Jia, J. J. Neumeier, J. Tesmer, J. D. Thompson, and X. D. Wu, Appl. Phys. Lett. **67**, 860 (1995); R. Mahendiran, A. K. Raychaudhuri, A. Chainani, D. D. Sarma, and S. B. Roy, *ibid.* **66**, 233 (1995).

[3] A. Asamitsu, Y. Moritomo, Y. Tomioka, T. Arima, and Y. Tokura, Nature (London) **373**, 407 (1995).

[4] H. L. Ju, C. Kwon, Qi Li, R. L. Greene, and T. Venkatesan, Appl. Phys. Lett. **65**, 2108 (1994) and references therein.

[5] A. Urushibara, Y. Moritomo, T. Arima, A. Asamitsu, G. Kido, and Y. Tokura, Phys. Rev. B **51**, 14 103 (1995).

[6] Guo-Meng Zhao, H. Keller, J. Hofer, A. Shengelaya, and K. A. Muller, Solid State Commun. **104**, 57 (1997).

[7] S. Jin, T. H. Tiefel, M. McCormack, R. A. Fastnacht, R. Ramesh, and L. H. Chen, Science **264**, 413 (1994).

[8] S. Jin, M. McCormack, T. H. Tiefel, and R. Ramesh, J. Appl. Phys. **76**, 6929 (1994).

[9] M. D. Struge, Phys. Rev. **140**, A880 (1965) and references therein; F. A. Cotton and G. Wilkinson, *Advanced Inorganic Chemistry* (Wiley, New York, 1972), p. 590.

[10] (a) D. Louca and T. Egami, J. Appl. Phys. **81**, 5484 (1997); (b) S. J. L. Billinge, R. G. DiFrancesco, G. H. Kwei, J. J. Neumeier, and J. D. Thompson, Phys. Rev. Lett. **77**, 715 (1996); (c) C. H. Booth, F. Bridges, G. J. Snyder, and T. H. Geballe, Phys. Rev. B **54**, 15 606 (1996); C. H. Booth, F. Bridges, G. H. Kwei, J. M. Lawrence, A. L. Cornelius, and J. J. Neumeier, Phys. Rev. Lett. **80**, 853 (1998); C. H. Booth *et al.* (unpublished); (d) T. A. Tyson, J. Mustre de Leon, S. D. Conradson, A. R. Bishop, J. J. Neumeier, H. Röder, and Jun Zang, Phys. Rev. B **53**, 13 985 (1996); (e) Changes in the long-range structure with temperature

were found by M. R. Ibarra, P. A. Algarabel, C. Marquina, J. Blasco, and J. Garcia, Phys. Rev. Lett. **75**, 3541 (1995).

[11] (a) C. Zener, Phys. Rev. **81**, 440 (1951); **82**, 403 (1951); (b) P. W. Anderson and H. Hasegawa, *ibid.* **100**, 675 (1955); (c) P.-G. de Gennes, *ibid.* **118**, 141 (1960); (d) K. Kubo and N. Ohata, J. Phys. Soc. Jpn. **33**, 21 (1972).

[12] M. F. Hundley and J. J. Neumeier, Phys. Rev. B **55**, 11 511 (1997).

[13] S. B. Oseroff, M. Torikachvili, J. Singley, S. Ali, S.-W. Cheong, and S. Schultz, Phys. Rev. B **53**, 6521 (1996).

[14] J.-H. Park, C. T. Chen, S-W. Cheong, W. Bao, G. Meigs, V. Chakarian, and Y. U. Idzerda, Phys. Rev. Lett. **76**, 4215 (1996).

[15] G. Subias, J. Garcia, M. G. Proietti, and J. Blasco, Phys. Rev. B **56**, 8183 (1997).

[16] (a) M. Croft, D. Sills, M. Greenblatt, C. Lee, S.-W. Cheong, K. V. Ramanujachary, and D. Tran, Phys. Rev. B **55**, 8726 (1997); (b) Z. Zeng, M. Greenblatt, and M. Croft, *ibid.* **58**, R595 (1998); Z. Zeng, M. Greenblatt, M. A. Subramanian, and M. Croft, Phys. Rev. Lett. **82**, 3164 (1999); A. Ramirez, P. Schiffer, S-W. Cheong, C. H. Chen, W. Bao, T. T. M. Palstra, B. Zegarski, P. L. Gammel, D. J. Bishop, and B. Zegarski, Phys. Rev. Lett. **76**, 3188 (1996); (c) P. Schiffer, A. Ramirez, W. Bao, and S.-W. Cheong, *ibid.* **75**, 3336 (1995).

[17] (a) R. S. Liu, J. B. Wu, C. Y. Chang, J. G. Lin, C. Y. Huang, J. M. Chen, and R. G. Liu, J. Solid State Chem. **125**, 112 (1996); (b) E. Pellegrin, L. H. Tjeng, F. M. F. de Groot, R. Hesper, G. A. Sawatzky, Y. Moritomo, and Y. Tokura, J. Electron Spectrosc. Relat. Phenom. **86**, 115 (1997).

[18] R. K. Singhal and K. B. Garg, J. Magn. Magn. Mater. **116**, 238 (1992); R. K. Singhal, U. Chandra, and K. B. Garg, *ibid.* **123**, 311 (1993).

[19] (a) G. Peng, F. M. F. de Groot, K. Hämäläinen, J. A. Moore, X. Wang, M. M. Grush, J. B. Hastings, D. P. Siddons, W. H. Armstrong, O. C. Mullins, and S. P. Cramer, J. Am. Chem. Soc. **116**, 2914 (1994) and references therein; (b) R. D. Cowan, *The Theory of Atomic Structure and Spectra* (University of California Press, Berkeley, 1981); (c) K. Tsutsumi, H. Nakamori, and K. Ichikawa, Phys. Rev. B **13**, 929 (1976) and references

therein; (d) see, for example, the case of Ti in *X-Ray Spectroscopy*, edited by L. V. Azaroff (McGraw Hill, New York, 1974), p. 507; (e) It should be noted that the peak normalization convention used here accentuates the very low intensity satellites of the higher valence spectra where the signal is low. In fact, in view of this, the discussion of the detailed variations in weak satellites of the higher valence spectra will be differed to further work.

[20] X. Wang, F. M. F. de Groot, and S. P. Cramer, Phys. Rev. B **56**, 4553 (1997).

[21] F. M. F. de Groot, A. Fontaine, C.-C. Kao, and M. Krisch, J. Phys.: Condens. Matter **6**, 6875 (1994).

[22] C.-C. Kao, K. Hämäläinen, M. Krisch, D. P. Siddons, T. Oversluizen, and J. B. Hastings, Rev. Sci. Instrum. **66**, 1699 (1995).

[23] (a) K. Hämäläinen, C.-C. Kao, J. B. Hastings, D. P. Siddons, L. E. Berman, V. Stojanoff, and S. P. Cramer, Phys. Rev. B **46**, 14 274 (1992); (b) K. Hämäläinen, D. P. Siddons, J. B. Hastings, and L. E. Berman, Phys. Rev. Lett. **67**, 2850 (1991).

[24] U. Bergmann, C. R. Horne, T. J. Collins, J. M. Workman, and S. P. Cramer, Chem. Phys. Lett. **302**, 119 (1999).